# Cretaceous age, composition and microstructure of pseudotachylyte in the Otago Schist, New Zealand

Running title: Pseudotachylyte in the Otago Schist

Shaun L.L. Barker[1*], J. Michael Palin[1], Richard H. Sibson[1], John D. FitzGerald[2], Steve Reddy[3], Laurence N. Warr[4] and Ben A. van der Pluijm[5]

[1] Department of Geology, University of Otago, P.O. Box 56, Dunedin, New Zealand

[2]Research School of Earth Sciences, The Australian National University, Canberra, ACT 0200, Australia

[3]The Institute for Geological Research, Department of Applied Geology, Curtin University of Technology, Perth, WA 6845, Australia

[4]Institute für Geographie und Geologie, Ernst Mortiz Arndt Universitaet Greifswald, Greifswald, Germany

[5]Department of Geological Sciences, University of Michigan, Ann Arbor, MI 48109-1005, U.S.A.

*Current address: Department of Earth and Ocean Sciences, University of British Columbia, Vancouver, BC V6T1Z4, Canada

e-mail: sbarker@eos.ubc.ca

Abstract

At Tucker Hill, in Central Otago, New Zealand, a series of pseudotachylyte veins are hosted in quartzofeldspathic schist. Chilled margins, microlites, flow banding, and the crystallisation of mineral phases absent from the host rock provide unequivocal evidence for melting during pseudotachylyte formation.

Whole rock analyses of pseudotachylyte reveal ~3x enrichment of $K_2O$, Ba and Rb, and similar depletion of $Na_2O$, CaO, Sr and Eu, as compared to host schist. Chemical profiles across one pseudotachylyte vein using laser-ablation. inductively-coupled-plasma, mass spectrometry indicate that variations in Rb, Ba, Sr and Cs concentrations of up to 50% occur between vein margin and centre.

Formation age of pseudotachylyte is 95.9 ± 1.8 Ma as measured by total fusion $^{40}Ar/^{39}Ar$ analyses. Stepwise heating of pseudotachylyte matrix yield an excellently defined $^{40}Ar/^{39}Ar$ plateau age of 96.0 ±0.3 Ma. We propose that formation of these pseudotachylyte veins was related to Cretaceous extensional uplift and exhumation of the Otago Schist.

39 1 Introduction

40

41 The presence of pseudotachylyte (former friction melt) in a fault zone is commonly
42 attributed to frictional melting of rock during seismic slip (Sibson, 1975). As such,
43 pseudotachylytes are valuable indicators that an exhumed fault zone was seismically active.
44 Pseudotachylytes have been described from inactive, ancient fault zones (e.g. Outer Hebrides
45 Fault Zone; Sibson, 1975; Maddock, 1983; Kelley et al., 1994) and present day seismically
46 active fault zones (e.g. the Alpine Fault; Sibson et al., 1981; Bossiere, 1991; Warr et al.,
47 2003). Determining the formation age of pseudotachylyte can reveal when a fault was
48 seismically active, and provide information on the regional significance of a
49 pseudotachylyte-bearing fault zone (Kelley et al., 1994; Magloughlin et al., 2001; Sherlock
50 & Hetzel, 2001; Mueller et al., 2002; Warr et al., 2003).

51 In Central Otago, New Zealand, a series of pseudotachylyte veins are found in schist
52 outcrop on Tucker Hill, near the township of Alexandra. The pseudotachylyte veins are
53 hosted in the garnet-biotite-albite zone of the greenschist facies of the Otago Schist,
54 which forms the basement rocks of much of the Otago region (Mortimer, 1993a,b). In
55 this study, we document the petrography and geochemistry of pseudotachylyte veins,
56 and present evidence for the origin of these pseudotachylyte veins as a friction melt. In
57 addition, we report laser ablation $^{40}Ar/^{39}Ar$ total fusion, single step infra red laser heating
58 ages, and stepwise heated $^{40}Ar/^{39}Ar$ analyses of fragments of pseudotachylyte matrix.

59 2 Geological Setting

60 The structural setting of the pseudotachylyte veins at Tucker Hill has been previously
61 described in Barker (2005). Briefly, more than 100 pseudotachylyte veins are distributed
62 throughout several cataclastic fault zones. The largest cataclastic fault zone, containing
63 shattered and incoherent schist is more than 400 m long, around 5-10 m thick, and dips
64 gently east with an unknown sense of displacement. In addition, several other
65 pseudotachylyte-bearing fault zones were mapped which strike NNW and dip east. The
66 majority of veins lie subparallel to schist foliation (Fig. 1a), and dip gently (between 10$^{o}$
67 and 30$^{o}$) towards the northeast. The length of fault veins is highly variable, with most
68 veins between 1 and 10 m long, and less than 2 cm thick. Slip sense indicators, in the
69 context of the veins present orientations, suggest that most veins have a top-to-the-north,
70 normal sense of shear.

71 The beginning of regional metamorphism for the Otago Schist has been inferred at ca.
72 199 Ma (Adams et al., 1985). Mortimer & Cooper (2004) suggest that the timing of
73 highest-grade metamorphic mineral growth in the Otago Schist was during the Jurassic.
74 Little et al. (1999) inferred that peak metamorphism in the Otago Schist occurred in the
75 middle Jurassic (170-180 Ma), and that the Otago Schist was held at mid to lower crustal
76 depths until 135 Ma. Thereafter, uplift occurred rapidly at 0.6–1 mm yr$^{-1}$ (Little et al.,
77 1999). Uplift and exhumation of the schist was accompanied by regional extension, and the
78 development of low-angle ductile shear zones at 135-105 Ma (Deckert et al., 2002; Forster &
79 Lister, 2003). Continuing extension in the mid Cretaceous led to the development of
80 brittle normal faults with a NW/SE and NE/SW oriented orthogonal pattern (Craw &
81 Norris, 1991). Overlying volcanic sediments suggest that deep levels of the Otago Schist had
82 been exposed by the mid to late Cretaceous (Adams & Raine, 1988). Neither the Rise and
83 Shine Shear Zone, nor the Cromwell Gorge Shear Zone displace the Waipounamu Erosion

Surface (LeMasurier & Landis, 1996), suggesting that shear zone displacement was complete by 105-85 Ma.

These pseudotachylyte veins do not appear to have any metamorphic overprint, and crosscut all metamorphic fabrics. The oldest apatite fission track ages from a nearby area (Tippett & Kamp; 1993) suggest that these rocks were near surface by c. 96–86 Ma. Thus, a geologically reasonable age for pseudotachylyte formation is considered to lie between 135 and 85 Ma.

Several thick pseudotachylyte veins were collected in the field, and three which showed unequivocal evidence for melting (e.g. chill margins) were selected for geochemical analysis (those rejected showed evidence for cataclasis, or were too small to provide enough material for geochemical analyses). These 3 veins (samples OU74171, OU 74172, OU 74178) were crushed and analysed for bulk rock by X-ray fluorescence (XRF) and laser ablation inductively coupled plasma mass spectrometry (LA-ICP-MS). Additionally, Ar-Ar geochronology was performed both on an intact-rock section (laser ablation) and selected fragments (stepwise heating) of OU74171. Nine host schist samples were also chosen from the Tucker Hill field area for comparison. Fresh samples were chosen, that is rocks with no macro or microscopic evidence for alteration.

## 2 Analytical methods

### *XRF*

Wall rock was trimmed from the edges of pseudotachylyte veins using a diamond saw and grindstone, and the veins were then crushed in a tungsten carbide swing mill. Resulting powders were then turned into fused (major elements) or pressed powder

(trace element) discs for analysis. Trace element analyses were carried out on pressed powder discs, using the procedures of Norrish and Chappell (1967). Trace element XRF analyses were checked for accuracy using a subset of international standards (Govindavaju, 1994). Analyses were conducted on a Phillips PW-2400 Automated Sequential XRF Spectrometer in the Department of Geology, University of Otago.

*LA-ICP-MS*

One pseudotachylyte sample (OU 74171) and its adjacent host rock (OU 74179) were chosen for LA-ICP-MS analysis. These samples were crushed in an agate swing mill, and were then fused into glass. Analyses were carried out on an Agilent 7500 quadrupole ICP-MS at the Research School of Earth Sciences, The Australian National University. A pulsed Lambola Physik LPX 1201 ArF excimer laser operated at a constant energy, and a 5 Hz pulse rate was used to ablate material from the surface of the whole rock glass discs. A laser spot width of 70 $\mu$m was used during spot analyses of schist and pseudotachylyte fused whole rock samples.

Data reduction followed established protocols for time-resolved analysis (Longerich et al., 1996), utilizing $SiO_2$ as an internal standard. Concentrations of $SiO_2$ determined by XRF analyses for schist and pseudotachylyte were used for LA-ICP-MS data reduction. The NIST 612 standard (values of Pearce et al, 1997), was analyzed before and after every 6 analyses for standardization.

*Electron microscopy*

One transmission electron microscope (TEM) specimen was prepared using standard petrographic thin section techniques, leading to extraction of a 3 mm disc of rock and

Argon-ion milling. Thin regions were dominantly found in the chlorite-rich matrix areas of the specimen. Transmission electron microscope observations were made at 300 kV using a Philips CM300 TEM (1999) based at the Research School of Earth Sciences, The Australian National University. Scanning electron microscope (SEM) observations on polished specimens were made on a Cambridge S360 SEM (1987) in the Electron Microscope Unit, The Australian National University.

A whole rock powder X-ray diffraction (XRD) analysis was carried out on one pseudotachylyte vein. X-ray diffraction was carried out with a SIEMENS D5005 Bragg-Brentano diffractometer based in the Department of Geology, Australian National University.

*Ar-Ar geochronology*

For laser ablation Ar-Ar geochronology, a thin section of pseudotachylyte was examined, and an area of matrix chosen and marked for analysis (e.g. an area free of lithic clasts). The sample was wrapped in aluminium foil and loaded into an aluminium package with biotite age standard HD-B1 (24.21 ± 0.32 Ma) to monitor the neutron flux gradient of the reactor (McMaster University Nuclear Reactor, Hamilton, Canada).

Argon analyses were undertaken at the Western Australian Argon Isotope Facility, Curtin University of Technology. Argon data were collected by single step, total fusion infra-red laser heating of the thick polished pseudotachylyte sample. A 110 W Spectron Laser Systems (CW-Nd-YAG laser ($\lambda$ = 1064 nm) was used to fuse individual c. 50 $\mu$m spots of the fault rock sample. Laser analyses were attempted from fine-grained, clast-free areas of pseudotachylyte matrix. Gases released by fusion were released into a high sensitivity mass spectrometer (MAP 215-50). Data were corrected for mass

spectrometer discrimination and nuclear interference reactions. The J value for the irradiation was 0.003565 ± 0.000018. $^{40}Ar/^{39}Ar$ ages were calculated using the decay constant of Steiger & Jaeger (1977).

For "intact rock" stepwise heating $^{40}Ar/^{39}Ar$ analysis, selected fragments of pseudotachylyte matrix were irradiated in the McMaster Nuclear Reactor (Canada). Unencapsulated samples were wrapped in aluminium foil and loaded into fused silica tubing for neutron irradiation. Encapsulated samples were analyzed using the method described in Dong *et al*. (1995). The encapsulated samples were placed into fused silica breakseal tubes which were subsequently evacuated to *ca*. 5 x $10^{-8}$ Torr. The connections to the breakseals were then collapsed while under vacuum. After neutron irradiation, the capsules were placed into a glass manifold connected to the VG1200S mass spectrometer at the University of Michigan. Upon breaking the fused silica vials, the recoil gas fraction can be analyzed on the mass spectrometer. All samples were step-heated using the defocused beam from a 5W argon-ion continuous laser, and the ages quoted are relative to an age of 27.99 Ma for standard biotite FCT-3, which in turn is relative to an age of 520.4 Ma for a standard hornblende MMhb-1 (Hall & Farrell, 1995).

## Sample Descriptions

### 3.1 Host Schist Petrography

Schist can be separated into two dominant lithologic components, quartz segregation bands and melanocratic bands. Segregation bands are composed of large, moderately to highly strained quartz grains, with minor albitic plagioclase, and rare muscovite, epidote and chlorite. Melanocratic bands have a larger proportion of plagioclase than quartz

175 segregation bands, with muscovite, chlorite and epidote also present. More rarely,
176 titanite (both metamorphic and relict detrital grains), detrital zircon, apatite, and
177 tourmaline are observed in melanocratic bands. Long, dusty streaks of fine-grained
178 graphite occur in all schist thin sections.

179 3.2 Pseudotachylyte Petrography

180 Macroscopically, lithic clasts of quartz (and minor schist) up to 5 mm are present within
181 pseudotachylyte veins. Dark margins are noticeable at the edges of many thick
182 pseudotachylyte veins, and one thick vein shows evidence for repeated melt episodes,
183 with multiple sets of dark margins, and mutual crosscutting relations preserved (Fig. 1).
184 Three components dominate the pseudotachylyte. These are:

185 (1) Lithic clasts: Remnant mineral and rock fragments from schist (Fig. 1c).

186 (2) Grains that crystallised from the pseudotachylyte melt, which can be resolved by
187 optical microscopy (> 2 $\mu$m; Fig. 1c).

188 (3) Fine-grained matrix (≤ 2 $\mu$m).

189 Most lithic clasts within the pseudotachylytes are quartz grains or aggregates, and are
190 variable in size (2 $\mu$m to greater than 1 mm). Quartz lithic clasts are scattered relatively
191 uniformly throughout thin fault veins. In thick veins, quartz lithic clasts are most
192 abundant within the dark margins. Small quartz clasts (< 100 $\mu$m) are usually well
193 rounded and intact. Larger quartz clasts are commonly more angular and contain
194 fractures, some of which are filled with former melt (Fig. 2a). Some quartz clasts
195 display diffuse rims in both optical light microscopy and SEM (Fig. 2b). Small quartz
196 clasts (<10 $\mu$m) are more commonly affected by such rims than larger quartz grains.
197 Quartz lithic clasts show rare embayments, where melt has intruded them. Plagioclase is

198 a minor lithic clast in the pseudotachylytes compared to quartz, and its modal
199 proportion is estimated to be < 1% of total pseudotachylyte volume (Fig. 2c).

200 Small (typically 1-5 $\mu$m wide, 10-50 $\mu$m long), tabular crystals of potassium
201 feldspar (characteristic XRD peaks at 3.22, 3.26 and 3.27 Å) occur in pseudotachylyte
202 veins ≥ 0.5 cm in width. Potassium feldspar microlites are absent in the chill margins of
203 veins, and become more abundant towards the centres of veins (Fig. 1c, confirmed by
204 electron diffraction in TEM). Measurements made using EDS via the TEM suggest that
205 the chemistry of potassium feldspar crystals changes little throughout the
206 pseudotachylyte. Many quartz and plagioclase lithic clasts are radially overgrown by
207 potassium feldspar microlites, and potassium feldspar infills small fractures in
208 plagioclase lithic clasts. Overgrowths and infills appear to be coeval with microlite
209 growth.

210 Chlorite forms the majority of matrix material between potassium feldspar
211 microlites (Figs. 1c, 2b, 3). Selected area electron diffraction of chlorite reveals
212 characteristic lattice spacing of 14 Å. Ultra-fine grained chlorite occurs as sharp, tabular
213 chlorite crystals, which are typically 50 to 100 nm wide, and 1 to 2 $\mu$m long (Fig. 3,
214 confirmed by electron diffraction in TEM). It is suggested that the chlorite crystallised
215 from a former glassy matrix.

216 Spherical structures, here referred to as spheroids, are found in all thick pseudotachylyte
217 veins examined during this study. These spheroids range from 10 $\mu$m to 300 $\mu$m in
218 diameter. Spheroids are not found in the dark margins of veins, and are larger and more
219 numerous towards the centre of veins. Spheroids are filled with a consistent mineral
220 assemblage, comprising quartz, titanite ± potassium feldspar ± chlorite (Fig. 4a).
221 Graphite is present in many of the spheroids, and occurs as a thin opaque (~1 $\mu$m) rim.

222 Chlorite occurs as low relief, light green plates, and is often found projecting from the
223 rim towards the centre of the spheroid. Titanite grains in spheroids grow to a relatively
224 large size (up to 50 $\mu$m), and often have a radial, zoned appearance (Figs. 4b and 4c).
225 The spheroids have similarities to amygdules in pseudotachylytes described by
226 Maddock et al. (1987).

227 4 Results

228 4.1 Geochemistry

229 Results obtained for whole rock major oxide XRF analyses of host schist and
230 pseudotachylyte are presented in Table 1. $Fe_2O_3$, MgO, CaO, $Na_2O$ and $K_2O$ show
231 greater concentration variability between schist samples than $SiO_2$, $TiO_2$ and $Al_2O_3$.
232 Greater variation for these elements is likely due to minor variations in mineral content
233 (e.g. muscovite, chlorite, plagioclase) between schist samples. Sample OU 74185 has a
234 higher $SiO_2$ content (66%), with a higher content of quartz segregation bands diluting
235 concentrations of other elements. Major and trace element compositions of Tucker Hill
236 schist agree well with those of schists previously analysed from Alexandra by Mortimer
237 and Roser (1992).

238 Whole rock XRF results reveal that the pseudotachylyte and schist samples have
239 approximately the same $SiO_2$, $Al_2O_3$ $Fe_2O_3$ and MgO concentrations (Fig. 5a). CaO and
240 $Na_2O$ contents are significantly lower in pseudotachylyte samples than they are in the
241 schist samples, while $K_2O$ is higher in pseudotachylyte. The trace elements Sc, V, Cr,
242 Ni, Cu, Zn, Ga, As, Rb, Sr, Y, Zr, Nb, Ba, La, Ce, Nd, Pb, Th and U were analysed by
243 XRF (Table 2; plotted as ratios in Fig. 5b). The most notable differences between
244 pseudotachylyte and schist are the increases in Ba and Rb concentrations, and the

245 decrease in Sr, Ga, As and Y in pseudotachylyte as compared to the host schist. The
246 trace elements Sc, V, Cr, Co, Ni, Cu, Rb, Sr, Y, Zr, Nb, Cs, Ba, La, Ce, Pr, Nd, Sm, Eu,
247 Gd, Tb, Dy, Er, Yb, Lu, Ta, Pb, Th and U were determined by LA-ICP-MS on whole
248 rock glasses. The results for these analyses are presented in Tables 3a and 3b, with
249 pseudotachylyte/schist ratios summarised in Figure 6a. The results obtained by LA-ICP-
250 MS agree well with those obtained by XRF. Notably, europium is lower by a factor of 3
251 in pseudotachylyte. A plot showing rare earth element (REE) concentrations normalised
252 to chondrite (values of McDonough and Sun, 1995) demonstrates that schist and
253 pseudotachylyte have almost identical REE patterns, excepting Eu which shows a
254 marked negative anomaly in pseudotachylyte (Fig. 6b).

255 4.2 Ar-Ar geochronology

256 Argon release spectra for both samples (encapsulated and unencapsulated) show comparable
257 degassing curves (Fig. 7). Minor disturbances during the release of $^{39}Ar$ occur at low
258 temperatures, followed by the formation of a well-developed plateau. The small
259 (0.0008 g) encapsulated fragment gave a total gas age of 95.95 Ma, and had a small
260 amount of recoiled $^{39}Ar$ (1.1 %). Variable and younger ages at low gas release temperatures
261 are associated with higher Cl/K and Ca/K. The remaining ~ 85% of degassed $^{39}Ar$
262 forms a rough plateau at ca. 96 Ma. At higher temperatures (final 10% of $^{39}Ar$ gas
263 released) fluctuating Cl/K and Ca/K are observed, but are not associated with strong
264 variations in calculated ages.
265 A larger sample (not encapsulated) produced an excellent $^{40}Ar/^{39}Ar$ plateau age of 95.85 ±0.70
266 Ma, which is defined by ca. 75% of degassed $^{39}Ar$. A similar total gas age of 95.44 ±0.17
267 Ma is determined. In detail, the stepwise release of the $^{39}Ar$ gas fraction shows minor

268 disturbance for the first 12 steps of heating, with slightly younger ages recorded for the first
269 30% of gas release. The first 3 steps produced significantly younger ages of <85 Ma, and are
270 associated with elevated Cl/K and Ca/K, with younger ages having higher ratios. All
271 other points of the spectrum show no relationship between age and Cl/K or Ca/K. The
272 average values for Cl/K and Ca/K are notably low for this sample (0.074 and 0.00045,
273 respectively).
274 For total-fusion Ar-Ar dating using laser ablation, twenty separate analyses were
275 attempted on one thin section. Of these, all but three analyses were abandoned due to
276 hydrocarbon interferences. The three completed analyses yield an unweighted mean age of
277 95.8 ±1.8 Ma (Table 4).
278

279 5. Discussion

280 5.1 Pseudotachylyte Melt Origin and Emplacement

281 Melting during pseudotachylyte formation is indicated by the presence of newly
282 crystallised phases, which are not found in the host schist (e.g. potassium feldspar),
283 igneous textures (e.g. fine grained microlites) and the presence of embayed lithic clasts.
284 The most abundant newly crystallised phase found in the Tucker Hill pseudotachylyte is
285 potassium feldspar. Potassium feldspar has not been reported from the Otago Schist,
286 either as a metamorphic mineral, or contained within mineralised veins (Youngson and
287 Craw, 1993). Thus, the presence of potassium feldspar in pseudotachylyte is strong
288 evidence for the formation and crystallisation of a melt.

289 In hand specimens, the outer margin of most thick (> 0.5 cm) veins has a thin (0.5 to 1
290 mm) black zone. When viewed in thin section, this margin is darker than the inner area

291 of the vein, contains no microlites, and very rare spheroids. We suggest that these dark
292 layers are chill margins, which formed when melt produced during pseudotachylyte
293 formation was rapidly cooled against the vein wall. The chill margins indicate that the
294 cooling times of the veins were sufficiently long to generate a temperature gradient
295 across the vein, with material nearer the middle of veins cooling slowly enough so that
296 potassium feldspar microlites could nucleate and grow. Several previous workers (e.g.
297 (Sibson, 1975; Maddock, 1983) have attributed chill margins to be a strong indicator for
298 the former presence of melt. Thin pseudotachylyte veins (< 0.5 cm) show no evidence
299 for chill margins, or the presence of potassium feldspar microlites. This suggests that
300 these thinner veins cool more quickly, with no opportunity for chill margin
301 development.

302 In several pseudotachylyte fault veins, lithic clasts show evidence for flow alignment,
303 with the long axes of quartz lithic clasts aligned subparallel to the walls of the
304 pseudotachylyte veins. This preferential alignment of lithic clasts suggests that there
305 was flow along veins during pseudotachylyte formation. In addition, macroscopic flow
306 banding has been noted in some pseudotachylyte veins (Fig. 8). Flow banding and
307 aligned lithic clasts suggest that friction melt viscosities were low enough (and cooling
308 times long enough) to allow melt to flow along veins. Injection veins (e.g. non-shear
309 surfaces) also require highly mobile melts, which can be rapidly injected from the
310 generating (shear) surface into the injection vein (Sibson, 1975).

311 5.2 Pseudotachylyte geochemistry

312 Pseudotachylyte compositions will be dependent on the mineralogy (and mineral
313 chemistry) of the host rock, the pressure-temperature-volatile conditions attained during
314 the melting process and possible mineral-melt separation processes. The

315 pseudotachylyte samples selected for analysis were separated by metres laterally and
316 vertically. Thus, there is little chance that they came from a single fault surface.
317 However, the similarity of pseudotachylyte compositions suggests that similar melting
318 conditions applied to each pseudotachylyte-generating event.

319 The major and trace elements most enriched in the pseudotachylyte, namely
320 $K_2O$, Rb and Ba have similar petrochemical behaviours which are distinct from those
321 most depleted in the pseudotachylyte (CaO, $Na_2O$ and Sr). Petrographic observations
322 suggest that the mineral in the schist most likely to contain significant concentrations of
323 $K_2O$, Ba and Rb is muscovite (NB – no biotite is present in the host schist), implying
324 that muscovite has been preferentially incorporated into pseudotachylyte during friction
325 melting (*cf*. Kelley et al, 1994). The mineral most likely to contain significant
326 concentrations of $Na_2O$, CaO, Sr and Eu is plagioclase. O'Hara (1992) also found
327 pseudotachylyte veins with markedly increased $K_2O$, and attributed this increase to
328 preferential melting of alkali feldspar. The results outlined above support both
329 experimental work (Spray, 1987; Spray, 1988; Spray, 1990; Spray, 1995) and
330 geochemical analyses of pseudotachylyte from impact craters (Killick, 1994; Thompson
331 and Spray, 1996) and fault-hosted pseudotachylyte (Maddock, 1992; Magloughlin,
332 1992; O'Hara, 1992; Camacho et al., 1995; O'Hara and Sharp, 2001). These previous
333 studies suggested that the formation of pseudotachylyte is accomplished by the
334 preferential melting of hydrous phases (e.g. micas, amphibole), and the preferential
335 retention, as lithic clasts, of plagioclase and quartz. The whole rock geochemical results
336 from this study demonstrate that there was preferential inclusion of a K-Rb-Ba bearing
337 phase(s) and preferential exclusion of a Ca-Na-Sr-Eu bearing phase(s) during
338 pseudotachylyte formation. The depletion of Sr and Eu strongly suggest that the phase

339 depleted from the pseudotachylyte is plagioclase, and not another Ca-bearing phase (i.e.
340 epidote, which may have a negative europium anomaly; Harlavan and Erel, 2002).

341 An alternative explanation for the pseudotachylyte composition is seritization of schist
342 host rock prior to pseudotachylyte formation. Seritization would cause enrichment of
343 $K_2O$, and depletion of $Na_2O$ and CaO. Studies of mid-ocean ridge hydrothermal systems
344 have established that mobilisation of REE occurs during such reactions, and a
345 pronounced positive Eu anomaly was observed in these hydrothermal solutions
346 (Douville et al., 2002). Therefore, it is possible that hydrothermal alteration could have
347 caused the geochemical differences observed between pseudotachylyte and unaltered
348 host schist. However, a significant amount of potassium metasomatism would have to
349 occur to cause the ~4 times increase in potassium concentrations observed (compared to
350 average schist). Whereas there is clear field evidence for hydrothermal alteration (quartz
351 and calcite veins) crosscutting pseudotachylyte in some parts of the field area, it is
352 unclear whether any hydrothermal alteration of schist occurred prior to pseudotachylyte
353 formation.

354 5.3 Ar-Ar geochronology

355 The two Ar-Ar geochronological methods yield statistically indistinguishable ages for the
356 formation of this pseudotachylyte vein. The argon release spectra obtained from the stepwise
357 heating method are excellent, and have more homogeneous plateaus than the results presented in
358 Magloughlin et al. (2001) and Mueller et al. (2002). This may be because the principal
359 potassium-bearing phase in this sample is potassium feldspar, and the sample contains no
360 biotite. Additionally, the sample appears to have few lithic clasts other than quartz and
361 plagioclase. Step-heating potassium feldspar is of particular value, because it remains stable

362 during heating under vacuum to the onset of melting. This sample clearly has neither lost
363 nor gained significant argon following the closure of the system, which is reflected in the
364 plateau age. There is also little recoil of argon. A key feature of this sample is its potassium
365 rich, Ca and Cl poor nature. This implies a low abundance of fluid inclusions, which can
366 contain extraneous argon. All of the above features make this pseudotachylyte vein an
367 excellent candidate for Ar-Ar geochronology.

368 The advantages of combining both stepwise heating of matrix fragments, and laser
369 ablation Ar-Ar techniques have been previously documented by both Magloughlin et al.
370 (2001) and Mueller et al. (2002). These two techniques allow melt-related ages to be
371 derived from potentially complex age spectra. Here, we have demonstrated that a potassic
372 rich sample, containing little inherited host rock material (other than quartz and
373 plagioclase) can produce smooth stepwise heating spectra with plateau and total gas ages
374 that are indistinguishable from laser ablation spot Ar-Ar analyses.
375 The ages determined for pseudotachylyte formation are geologically compatible with regional
376 studies of the uplift and erosion of the Otago Schist belt. Previous studies have documented
377 the location and timing of ductile shear zone formation (Deckert et al., 2002; Forster &
378 Lister, 2003), brittle fault formation (Craw & Norris, 1991), uplift (Tippett & Kamp,
379 1993) and sedimentation in the Otago Schist. Prior to this study, the only direct evidence
380 for faulting of late Cretaceous age in the Otago region was in three areas where late
381 Cretaceous sedimentary rocks are preserved; the Kyeburn Formation, Henley Breccia
382 and Horse Range Formation (Bishop and Laird, 1976; Bishop and Tulloch 1996,
383 Forsyth, 2001). The Kyeburn and Horse Range Formations have been interpreted as
384 synorogenic sedimentary deposits, which contain tuffs that yield ages of 112 Ma
385 (Tulloch et al., in press).

We suggest that these pseudotachylyte veins were formed by seismic activity in the upper Cretaceous (Cenomanian), and may be related to the latest stages of the uplift and exhumation of the Otago Schist. This new age data provides unambiguous evidence for a Cretaceous fault in the Otago Schist ,with Ar-Ar geochronology specifically placing the age of pseudotachylyte formation at 96 Ma. This study raises the possibility that exhumation-related faults in the Otago Schist may be more widespread than previously suspected.

Acknowledgements

Nick Mortimer, Alan Cooper, Dave Craw, Doug Coombs, Stephen Cox, and other researchers have offered much useful advice and discussion during this research. Brent Pooley and Harri Kokkonen are thanked for assistance with petrographic preparation. This work was part of a BSc (Hons) project by S.L.L.B conducted at the Department of Geology, University of Otago. SLLB acknowledges a summer research scholarship from The Australian National University, during which much of this research was undertaken. This study was partially funded by the Marsden Fund (Contract UOO 216-"Fault rock studies on seismic and aseismic slip processes") administered by the Royal Society of New Zealand. The Ar-Ar research (Michigan) was supported by grants from the U.S. National Earthquake Hazards Reduction Program (USGS-04HQGR0066) and the U.S. National Science Foundation (EAR-0230055 and 0345985).

References

Adams, C., Bishop, D. & Gabites, J. 1985 Potassium-argon age studies

409 of a low-grade, progresively metamorphosed greywacke sequence, Dansey Pass, New
410 Zealand. Journal of the Geological Society of London 142, 339– 349.

411 Adams, C. & Raine, J. 1988 Age of Cretaceous silicic volcanism at Kye-burn, central
412 Otago, and Palmerston, eastern Otago, South Island, New Zealand. New Zealand Journal
413 of Geology and Geophysics 31 (4), 471–475.

414 Barker, S. 2005 Pseudotachylyte-generating faults in Central Otago, New Zealand.
415 Tectonophysics 397 (3-4), 211–223.
416 Bishop, D. G.; Laird, M. G. 1976. Stratigraphy and depositional environment of the
417 Kyeburn Formation (Cretaceous), a wedge of coarse terrestrial sediments in Central
418 Otago. Journal of the Royal Society of New Zealand 6: 55-71.
419
420 Bishop DG, Turnbull IM (compilers) 1996. Geology of the Dunedin area. Institute of
421 Geological & Nuclear Sciences 1:250 000 Geological Map 21. Institute of Geological &
422 Nuclear Sciences, Lower Hutt, New Zealand.

423 Bossiere, G. 1991 Petrology of pseudotachylytes from the Alpine Fault of New Zealand.
424 Tectonophysics 196 (1-2), 173–193.
425 Camacho, A., Vernon, R.H. and Fitz, G.J.D., 1995. Large volumes of anhydrous
426 pseudotachylyte in the Woodroffe Thrust, eastern Musgrave Ranges, Australia.
427 Journal of Structural Geology, 17(3): 371-383.

428 Craw, D. & Norris, R. 1991 Metamorphogenic Au-W veins and regional tectonics;
429 mineralisation throughout the uplift history of the Haast Schist, New Zealand. New
430 Zealand Journal of Geology and Geophysics 34 (3), 373–383.

431 Deckert, H., Ring, U. & Mortimer, N. 2002 Tectonic significance of Cretacoues
432 bivergent extensional shear zones in the Torlesse accretionary wedge, central Otago Schist,
433 New Zealand. New Zealand Journal of Geology and Geophysics 34, 373–383.

434 Dong, H., Hall, C., Peacor, D. & Halliday, A. 1995 Mechanisms of argon retention in
435 clays revealed by laser $^{40}Ar/^{39}Ar$ dating. Science 267 (5196), 355–359.
436 Forster, M. & Lister, G. 2003 Cretaceous metamorphic core complexes in the Otago
437 Schist, New Zealand. Australian Journal of Earth Sciences 50 (2), 181–198.
438 Forsyth PJ (compiler) 2001. Geology of the Waitaki area. Institute of Geological &
439 Nuclear Sciences 1:250 000 Geological Map 19. Institute of Geological & Nuclear
440 Sciences, Lower Hutt, New Zealand.
441 Govindavaju, K.A., 1994. A 1994 Compilation of working values and sample
442 description for 383 geostandards. Geostandards Newsletter, 1: 158.

443 Hall, C. & Farrell, J. 1995 Laser $^{40}Ar/^{39}Ar$ ar ages of tephra from Indian Ocean deep-sea
444 sediments; tie points for the astronomical and geomagnetic polarity time scales. Earth and
445 Planetary Science Letters 133 (3-4), 327– 338.
446 Harlavan, Y. and Erel, Y., 2002. The release of Pb and REE from granitoids by the
447 dissolution of accessory phases. Geochimica et Cosmochimica Acta, 66(5): 837-
448 848.

449 Kelley, S., Reddy, S. & Maddock, R. 1994 Laser-probe $^{40}Ar/^{39}Ar$ investigation of a
450 pseudotachylyte and its host rock from the Outer Isles Thrust, Scotland. Geology
451 (Boulder) 22 (5), 443–446.
452 Killick, A.M., 1994. The geochemistry of pseudotachylyte and its host rocks from the
453 West Rand Goldfield, Witwatersrand Basin, South Africa; implications for
454 pseudotachylyte genesis. Lithos, 32(3-4): 193-205.

455 LeMasurier, W. & Landis, C. 1996 Mantle-plume activity recorded by low-relief erosion
456 surfaces in West Antarctica and New Zealand. Geological Society of America Bulletin
457 108 (11), 1450–1466.

458 Little, T., Mortimer, N. & McWilliams, M. 1999 An episodic Cretaceous cooling model
459 for the Otago-Marlborough Schist, New Zealand, based on $^{40}Ar/^{39}Ar$ ar white mica ages.
460 New Zealand Journal of Geology and Geophysics 42 (3), 305–325.
461 Longerich, H., Jackson, S., Gunter, D., 1996. Laser ablation inductively coupled plasma
462 mass spectrometric transient signal data acquisition and analyte concentration
463 calculation. Journal of Analytical Atomic Spectrometry 11, 899–904.

464 Maddock, R. 1983 Melt origin of fault-generated pseudotachylytes demonstrated by
465 textures. Geology (Boulder) 11 (2), 105–108. Maddock, R., Grocott, J. & van Nes, M.
466 1987 Vesicles, amygdales and similar structures in fault-generated pseudotachylytes.
467 Lithos 20 (5), 419–432.
468 Maddock, R.H., 1992. Effects of lithology, cataclasis and melting on the composition of
469 fault-generated pseudotachylytes in Lewisian gneiss, Scotland. Tectonophysics.
470 Vol. 204 pp. 261-278.

471 Magloughlin, J., Hall, C. & van, d. 2001 $^{40}Ar/^{39}Ar$ geochronometry of pseudotachylytes by
472 vacuum encapsulation; North Cascade Mountains, Washington, USA. Geology
473 (Boulder) 29 (1), 51–54.
474 McDonough, W.F. and Sun, S.-s., 1995. The composition of the Earth. Chemical
475 Geology, vol. 120: 223-253.

476 Mortimer, N. 1993a Geology of the Otago Schist and adjacent rocks. scale 1: 500 000.

477 Mortimer, N. 1993b Jurassic tectonic history of the Otago Schist, New Zealand.
478 Tectonics 12 (1), 237–244.

479 Mortimer, N. & Cooper, A. 2004 U-Pb and Sm-Nd from the Alpine Schist, New Zealand.
480 New Zealand Journal of Geology and Geophysics 47, 21–28.
481 Mortimer, N. and Roser, B.P., 1992. Geochemical evidence for the position of the
482 Caples-Torlesse boundary in the Otago Schist, New Zealand. Journal of the
483 Geological Society of London, 149 Part 6: 967-977.

484 Mueller, W., Kelley, S. & Villa, I. 2002 Dating fault-generated pseu-dotachylytes;
485 comparison of $^{40}Ar/^{39}Ar$ stepwise-heating, laser-ablation and
486 Rb-Sr microsampling analyses. Contributions to Mineralogy and Petrology 144 (1), 57–
487 77.
488 Norrish, K. and Chappell, B., 1967. X-ray fluoresence spectrography. In: J. Zussman
489 (Editor), Physical Methods in Determinative Mineralogy. Academic Press,
490 London, pp. 161-214.

O'Hara, K., 1992. Major- and trace-element constraints on the petrogenesis of a fault-related pseudotachylyte, western Blue Ridge Province, North Carolina. Tectonophysics. vol. 204 pp. 279-288.

O'Hara, K.D. and Sharp, Z.D., 2001. Chemical and oxygen isotope composition of natural and artificial pseudotachylyte; role of water during frictional fusion. Earth and Planetary Science Letters, 184(2): 393-406.

Pearce, N.J.G., Perkins, W.T., Westgate, J.A., Gordon, M.P., Jackson, S.E. Neal, C.R. and Chenery, S.P. 2007. A compilation of new and published major and trace element data for NIST SRM 610 and NIST SRM 612 glass reference materials. Geostandards and Geoanalytical Research 21, 115-144

Sherlock, S. & Hetzel, R. 2001 A laser-probe $^{40}Ar/^{39}Ar$ study of pseudotachylite from the Tambach fault zone, Kenya; direct isotopic dating of brittle faults. Journal of Structural Geology 23 (1), 33–44.

Sibson, R. 1975 Generation of pseudotachylyte by ancient seismic faulting. The Geophysical Journal of the Royal Astronomical Society 43 (3), 775– 794.

Sibson, R., White, S. & Atkinson, B. 1981 Structure and distribution of fault rocks in the Alpine Fault Zone, New Zealand. In Thrust and nappe tectonics; International conference. (ed. McClay & R. . Price), Special Publication - Geological Society of London, vol. 9, pp. 197–210. London, United Kingdom: Geological Society of London.

Steiger, R. & Jaeger, E. 1977 Subcommission on geochronology; convention on the use of decay constants in geo- and cosmochronology. Earth and Planetary Science Letters 36 (3), 359–362.

514 Thompson, L.M. and Spray, J.G., 1996. Pseudotachylyte petrogenesis; constraints from
515 the Sudbury impact structure. Contributions to Mineralogy and Petrology, 125:
516 359-374.

517 Tippett, J. & Kamp, P. 1993 Fission track analysis of the late Ceno-zoic vertical
518 kinematics of continental pacific crust, Otago Schist, New Zealand. Journal of
519 Geophysical Research, B, Solid Earth and Planets 98 (9), 16,119–16,148.
520 Tulloch, AJ, Ramezani, J, Mortimer, N, Mortensen, J, van den Bogaard, P, Maas, R, in
521 press. Mid-Cretaceous felsic volcanism in New Zealand and Lord Howe Rise
522 (Zealandia) as a precursor to continental breakup. Geol Soc London Spec Paper.

523 Warr, L., van, d., Peacor, D. & Hall, C. 2003 Frictional melt pulses during a
524 approximately 1.1 Ma earthquake along the Alpine Fault, New Zealand. Earth and
525 Planetary Science Letters 209 (1-2), 39–52.

526 Youngson, J.H. and Craw, D., 1993. Gold nugget growth during tectonically induced
527 sedimentary recycling, Otago, New Zealand. Sedimentary Geology, 84(1-4): 71-88
528
529

Tables

**Table 1: Major element (wt%) concentrations for schist and pseudotachylyte from XRF analyses.**

| Sample | $SiO_2$ | $TiO_2$ | $Al_2O_3$ | $Fe_2O_3^t$ | MnO | MgO | CaO | $Na_2O$ | $K_2O$ | $P_2O_5$ | LOI | % Total |
|---|---|---|---|---|---|---|---|---|---|---|---|---|
| Schist 1 (OU74180) | 59.34 | 0.90 | 17.47 | 7.39 | 0.11 | 3.11 | 2.87 | 2.69 | 2.79 | 0.22 | 3.14 | 100.03 |
| Schist 2 (OU74181) | 60.55 | 0.79 | 18.06 | 5.86 | 0.08 | 2.08 | 3.43 | 3.96 | 2.35 | 0.21 | 2.63 | 100.00 |
| Schist 3 (OU74182) | 58.90 | 0.80 | 17.85 | 6.96 | 0.08 | 2.08 | 3.25 | 3.08 | 2.76 | 0.25 | 3.33 | 99.34 |
| Schist 4 (OU74183) | 60.55 | 0.83 | 17.06 | 6.48 | 0.09 | 2.33 | 4.01 | 3.97 | 1.92 | 0.21 | 2.41 | 99.86 |
| Schist 5 (OU74184) | 59.88 | 0.90 | 17.02 | 7.03 | 0.10 | 2.80 | 4.01 | 3.79 | 1.63 | 0.21 | 2.71 | 100.08 |
| Schist 6 (OU74185) | 66.51 | 0.70 | 14.51 | 5.33 | 0.08 | 1.96 | 3.01 | 3.21 | 1.94 | 0.20 | 2.17 | 99.62 |
| Schist 7 (OU74186) | 60.60 | 0.85 | 16.96 | 6.64 | 0.09 | 2.60 | 3.94 | 3.80 | 1.68 | 0.19 | 2.52 | 99.87 |
| Schist 8 (OU74187) | 57.53 | 0.87 | 18.50 | 6.78 | 0.09 | 2.32 | 4.84 | 3.14 | 2.88 | 0.21 | 2.81 | 99.97 |
| Schist 9 (OU74188) | 61.39 | 0.78 | 16.92 | 6.17 | 0.09 | 2.18 | 4.01 | 4.09 | 1.72 | 0.21 | 2.45 | 100.01 |
| Average | 60.58 | 0.82 | 17.15 | 6.52 | 0.09 | 2.38 | 3.71 | 3.53 | 2.19 | 0.21 | 2.69 | 99.86 |
| Standard Deviation | 2.50 | 0.06 | 1.14 | 0.64 | 0.01 | 0.38 | 0.62 | 0.50 | 0.51 | 0.02 | 0.36 | |
| | | | | | | | | | | | | |
| Pst. 1 (OU 74171) | 59.96 | 0.78 | 16.31 | 6.45 | 0.10 | 2.57 | 1.46 | 0.94 | 8.57 | 0.19 | 2.54 | 99.87 |
| Pst. 2 (OU 74172) | 58.54 | 0.78 | 16.58 | 6.33 | 0.10 | 2.50 | 1.81 | 0.86 | 9.39 | 0.19 | 2.77 | 99.85 |
| Pst. 3 (OU 74178) | 58.46 | 0.79 | 16.90 | 6.38 | 0.09 | 2.45 | 1.50 | 0.88 | 9.39 | 0.19 | 2.56 | 99.59 |
| Average | 58.99 | 0.78 | 16.60 | 6.39 | 0.10 | 2.51 | 1.59 | 0.89 | 9.12 | 0.19 | 2.62 | 99.77 |
| Standard Deviation | 0.84 | 0.01 | 0.30 | 0.06 | 0.01 | 0.06 | 0.19 | 0.04 | 0.47 | 0.00 | 0.13 | |

**Table 2: Trace element (mg/kg) composition of schist and pseudotachylyte from XRF analyses.**

| Sample | Sc | V | Cr | Ni | Cu | Zn | Ga | As | Rb | Sr | Y | Zr | Nb | Ba | La | Ce | Nd | Pb | Th | U |
|---|---|---|---|---|---|---|---|---|---|---|---|---|---|---|---|---|---|---|---|---|
| Schist 1 (OU74180) | 14 | 151 | 51 | 18 | 39 | 88 | 21 | 5 | 92 | 384 | 22 | 156 | 9 | 673 | 18 | 53 | 30 | 23 | 11 | 5 |
| Schist 2 (OU74181) | 13 | 133 | 43 | 16 | 20 | 80 | 20 | 7 | 81 | 401 | 22 | 176 | 8 | 558 | 18 | 45 | 23 | 16 | 11 | 4 |
| Schist 3 (OU74182) | 12 | 119 | 37 | 15 | 19 | 74 | 17 | 8 | 65 | 365 | 19 | 155 | 6 | 585 | 16 | 32 | 15 | 21 | 8 | 4 |
| Schist 4 (OU74183) | 16 | 152 | 52 | 18 | 27 | 82 | 19 | 10 | 63 | 491 | 21 | 162 | 7 | 541 | 15 | 40 | 19 | 17 | 7 | 3 |
| Schist 5 (OU74184) | 15 | 152 | 54 | 18 | 39 | 88 | 20 | 4 | 92 | 383 | 22 | 156 | 9 | 679 | 19 | 51 | 25 | 24 | 10 | 4 |
| Schist 6 (OU74185) | 17 | 170 | 52 | 19 | 25 | 83 | 19 | 17 | 53 | 471 | 19 | 149 | 7 | 512 | 22 | 36 | 23 | 14 | 8 | 3 |
| Schist 7 (OU74186) | 16 | 141 | 49 | 17 | 35 | 75 | 20 | 7 | 57 | 480 | 22 | 164 | 6 | 492 | 22 | 56 | 19 | 18 | 7 | 3 |
| Schist 8 (OU74187) | 16 | 155 | 44 | 15 | 44 | 72 | 22 | 8 | 84 | 591 | 22 | 172 | 9 | 699 | 17 | 47 | 20 | 17 | 9 | 4 |
| Schist 9 (OU74188) | 14 | 157 | 48 | 17 | 38 | 76 | 19 | 11 | 56 | 474 | 20 | 151 | 6 | 516 | 18 | 34 | 19 | 16 | 7 | 4 |
| **Average=** | 15 | 148 | 48 | 17 | 32 | 80 | 20 | 9 | 71 | 449 | 21 | 160 | 7 | 584 | 18 | 44 | 21 | 18 | 9 | 4 |
| | | | | | | | | | | | | | | | | | | | | |
| Pst. 1 (OU 74171) | 12 | 131 | 37 | 18 | 32 | 76 | 13 | 5 | 209 | 270 | 13 | 152 | 9 | 1670 | 18 | 48 | 18 | 22 | 7 | 3 |
| Pst. 2 (OU 74172) | 14 | 126 | 37 | 18 | 32 | 74 | 13 | 5 | 226 | 260 | 12 | 148 | 10 | 1480 | 17 | 44 | 25 | 20 | 9 | 4 |
| Pst. 3 (OU 74178) | 14 | 135 | 38 | 18 | 40 | 76 | 13 | 4 | 215 | 237 | 13 | 145 | 12 | 2069 | 15 | 47 | 24 | 19 | 9 | 4 |
| **Average=** | 14 | 131 | 38 | 18 | 36 | 75 | 13 | 5 | 221 | 249 | 13 | 147 | 11 | 1775 | 16 | 46 | 25 | 20 | 9 | 4 |

**Table 3: Trace element composition (mg/kg) of pseudotachylyte and schist whole rock glasses as determined by LA-ICP-MS, for separate spot analyses carried out on fused samples for elements Sc to La. Ce to U on following page.**

| Sample | $SiO_2$ (wt%) | Sc | V | Cr | Co | Ni | Cu | Rb | Sr | Y | Zr | Nb | Cs | Ba | La |
|---|---|---|---|---|---|---|---|---|---|---|---|---|---|---|---|
| Schist Glass 1a | 60.6 | 22.2 | 165 | 41.3 | 13.9 | 13.7 | 16.0 | 57.8 | 551 | 24.3 | 179 | 7.1 | 2.6 | 464 | 24.8 |
| Schist Glass 1b | 60.6 | 17.0 | 136 | 32.5 | 11.0 | 10.7 | 14.5 | 64.6 | 440 | 18.4 | 133 | 6.3 | 3.6 | 392 | 19.3 |
| Schist Glass 1c | 60.6 | 22.4 | 172 | 44.5 | 15.4 | 14.9 | 19.9 | 60.8 | 542 | 24.7 | 191 | 7.5 | 3.2 | 462 | 25.8 |
| Schist Glass 1d | 60.6 | 21.2 | 137 | 38.1 | 10.7 | 10.6 | 13.3 | 66.2 | 506 | 23.4 | 154 | 6.6 | 3.7 | 439 | 24.3 |
| Schist Glass 1e | 60.6 | 21.3 | 164 | 41.7 | 12.0 | 12.3 | 14.2 | 67.7 | 533 | 23.7 | 160 | 8.3 | 3.8 | 459 | 24.7 |
| Schist Glass 1f | 60.6 | 20.5 | 161 | 40.4 | 13.6 | 13.6 | 20.0 | 64.9 | 545 | 23.4 | 182 | 7.7 | 3.6 | 472 | 25.0 |
| Average= | 60.6 | 20.7 | 156 | 39.7 | 12.7 | 12.6 | 16.3 | 63.7 | 520 | 23.0 | 166 | 7.3 | 3.4 | 448 | 24.0 |
| | | | | | | | | | | | | | | | |
| Pseudotachylyte 2a | 59 | 16.5 | 129 | 39.1 | 13.6 | 15.1 | 22.8 | 225 | 240 | 18.7 | 143 | 6.2 | 2.1 | 1840 | 18.2 |
| Pseudotachylyte 2b | 59 | 16.0 | 128 | 38.8 | 13.3 | 14.7 | 21.6 | 238 | 230 | 17.7 | 139 | 6.1 | 2.5 | 1790 | 17.5 |
| Pseudotachylyte 2c | 59 | 16.3 | 127 | 39.2 | 13.6 | 15.4 | 22.0 | 203 | 234 | 18.2 | 137 | 6.2 | 1.7 | 1810 | 17.7 |
| Pseudotachylyte 2d | 59 | 16.6 | 129 | 38.7 | 14.2 | 15.8 | 23.0 | 264 | 238 | 18.8 | 146 | 6.6 | 2.8 | 1860 | 18.4 |
| Pseudotachylyte 2e | 59 | 16.2 | 130 | 39.1 | 14.0 | 16.6 | 24.3 | 240 | 239 | 18.5 | 143 | 6.6 | 2.1 | 1900 | 18.4 |
| Pseudotachylyte 2f | 59 | 16.0 | 131 | 38.6 | 13.7 | 15.5 | 23.7 | 255 | 235 | 18.2 | 150 | 6.7 | 2.7 | 1900 | 18.8 |
| Average= | 59 | 16.2 | 129 | 38.9 | 13.7 | 15.5 | 22.9 | 237 | 236 | 18.4 | 143 | 6.4 | 2.3 | 1850 | 18.2 |

**Table 3 (continued): Elements Ce to U**

| Sample | Ce | Pr | Nd | Sm | Eu | Gd | Tb | Dy | Er | Yb | Lu | Ta | Pb | Th | U |
|---|---|---|---|---|---|---|---|---|---|---|---|---|---|---|---|
| Schist Glass 1a | 54.9 | 6.6 | 24.1 | 5.6 | 1.49 | 5.0 | 0.77 | 4.8 | 2.7 | 2.6 | 0.40 | 0.58 | 18.9 | 9.3 | 2.3 |
| Schist Glass 1b | 42.8 | 5.1 | 18.7 | 4.3 | 1.14 | 3.9 | 0.57 | 3.7 | 2.1 | 2.1 | 0.30 | 0.50 | 14.3 | 7.2 | 1.9 |
| Schist Glass 1c | 57.1 | 6.8 | 25.1 | 5.8 | 1.51 | 5.3 | 0.78 | 4.9 | 2.9 | 2.8 | 0.42 | 0.60 | 18.1 | 9.5 | 2.4 |
| Schist Glass 1d | 54.1 | 6.4 | 23.9 | 5.4 | 1.53 | 4.9 | 0.72 | 4.7 | 2.6 | 2.6 | 0.37 | 0.55 | 13.2 | 9.0 | 2.3 |
| Schist Glass 1e | 55.0 | 6.5 | 24.3 | 5.5 | 1.50 | 5.1 | 0.73 | 4.7 | 2.6 | 2.6 | 0.40 | 0.67 | 16.1 | 9.3 | 2.4 |
| Schist Glass 1f | 55.2 | 6.5 | 24.4 | 5.7 | 1.46 | 5.1 | 0.74 | 4.7 | 2.7 | 2.7 | 0.41 | 0.64 | 18.5 | 9.3 | 2.4 |
| Average= | 53.2 | 6.3 | 23.4 | 5.4 | 1.44 | 4.9 | 0.72 | 4.6 | 2.6 | 2.6 | 0.39 | 0.59 | 16.5 | 8.9 | 2.3 |
| | | | | | | | | | | | | | | | |
| Pseudotachylyte 2a | 42.3 | 5.1 | 18.9 | 4.3 | 0.47 | 4.1 | 0.57 | 3.6 | 2.1 | 2.1 | 0.32 | 0.50 | 22.8 | 7.9 | 1.8 |
| Pseudotachylyte 2b | 40.7 | 4.8 | 18.0 | 4.2 | 0.46 | 3.8 | 0.57 | 3.4 | 2.1 | 2.0 | 0.30 | 0.50 | 25.2 | 7.9 | 1.9 |
| Pseudotachylyte 2c | 41.3 | 4.9 | 18.6 | 4.4 | 0.48 | 4.0 | 0.57 | 3.7 | 2.1 | 2.1 | 0.33 | 0.50 | 16.6 | 8.1 | 1.9 |
| Pseudotachylyte 2d | 42.7 | 5.0 | 18.9 | 4.4 | 0.52 | 4.0 | 0.59 | 3.7 | 2.1 | 2.1 | 0.33 | 0.51 | 27.0 | 8.1 | 1.9 |
| Pseudotachylyte 2e | 42.8 | 5.1 | 19.0 | 4.4 | 0.51 | 4.0 | 0.60 | 3.8 | 2.1 | 2.2 | 0.33 | 0.53 | 27.5 | 8.2 | 1.9 |
| Pseudotachylyte 2f | 43.8 | 5.2 | 19.4 | 4.5 | 0.51 | 4.0 | 0.59 | 3.8 | 2.2 | 2.3 | 0.33 | 0.56 | 29.4 | 8.4 | 2.0 |
| Average= | 42.3 | 5.0 | 18.8 | 4.4 | 0.49 | 4.0 | 0.58 | 3.7 | 2.1 | 2.1 | 0.32 | 0.52 | 24.8 | 8.1 | 1.9 |

**Table 4: Results from laser ablation Ar-Ar analyses.**

| Sample no. | $^{40}Ar/^{39}Ar$ | ± | $^{38}Ar/^{39}Ar$ | ± | $^{37}Ar/^{39}Ar$ | ± | $^{36}Ar/^{39}Ar$ | ± | $^{39}Ar$ ($cm^3$) | ± | $^{40}Ar^*/^{39}Ar$ | ± | Age (Ma) | ± |
|---|---|---|---|---|---|---|---|---|---|---|---|---|---|---|
| OU74172-1 | 22.22036 | 0.04138 | 0.01719 | 0.00028 | 0.40077 | 0.15314 | 0.02199 | 0.00079 | 1.09E-11 | 1.65E-14 | 15.72151 | 0.23445 | **98.4** | **1.5** |
| OU74172-2 | 23.91910 | 0.02996 | 0.01722 | 0.00021 | 0.50640 | 0.05374 | 0.02987 | 0.00033 | 1.48E-11 | 1.12E-14 | 15.09113 | 0.10128 | **94.5** | **0.8** |
| OU74172-3 | 22.49993 | 0.05032 | 0.01711 | 0.00041 | 0.70186 | 0.10989 | 0.02494 | 0.00066 | 7.39E-12 | 6.06E-15 | 15.13125 | 0.20124 | **94.8** | **1.3** |
| unweighted mean | | | | | | | | | | | | | 95.9 | 1.8 |
| weighted mean | | | | | | | | | | | | | 95.2 | 0.6 |

Figure Captions

Figure 1: (a) Typical thick (*ca*. 1 cm thick) pseudotachylyte vein in outcrop formed of schist host rock. Note pen (15 cm long) for scale.

(b) Thickest pseudotachylyte vein found at Tucker Hill (*ca*. 5 cm thick) examined in thin section. Note several sets of chill margins and quartz lithic clasts. Ruler (cm markings) for scale.

(c) Photomicrograph showing a typical margin of a pseudotachylyte vein. Note numerous lithic clasts, especially in margin of vein. Tiny potassium feldspar microlites (10 $\mu$m scale) can be seen in to right side of photomicrograph, away from chill margin.

Figure 2: (a) SEM backscattered electron photomicrograph showing a typical fractured quartz lithic clast. Note lighter grey melt phase infilling crack, and barren crack (from top of lithic clast).

(b) Photomicrograph in plane polarised light showing a blurry rimmed lithic clast.

(c) SEM photomicrograph showing an indistinct rimmed plagioclase (plg) lithic clast, onto which potassium feldspar microlites are growing.

Figure 3: TEM brightfield photomicrograph showing a mat of fine-grained chlorite in a matrix area of pseudotachylyte.

Figure 4: (a) Photomicrograph in plane polarised light showing spheroids in OU 74178. Note dark black graphite rim on edge of spheroids, and titanite (dark brown, very high relief, laballed "tit") growing from edges of spheroid towards centre.

(b) SEM backscatteed electron photomicrograph showing radial morphology of a titanite contained within an spheroid. Titanite appears to nucleate from a point to the bottom right of photomicrograph.

(c) Photomicrograph in plane polarised light showing spheroids in OU 74178. Note colour zoning within titanites, and both quartz (dominant infilling material in large, central spheroid) and potassium feldspar (right hand side of large, central spheroid).

Figure 5: (a) Comparison of pseudotachylyte and schist major element XRF compositions. To illustrate the size and significance of these compositional variations between pseudotachylyte and host schist concentration ratios have been calculated with errors included using standard propagation techniques. This is as follows: if R is the ratio of the average concentration of an element in schist and pseudotachylyte:

$$R = \frac{\text{pseudotachylyte concentration}}{\text{schist concentration}}$$

then the error (e) associated with R is:

$$e = R \times \left( \left( \frac{\text{pseudotachylyte SD}}{\text{pseudotachylyte } \bar{x} \text{ concentration}} \right)^2 + \left( \frac{\text{schist SD}}{\text{schist } \bar{x} \text{ concentration}} \right)^2 \right)^{0.5},$$

where SD= standard deviation of all analyses.

Values of R greater than 1 indicate enrichment of an element in pseudotachylyte relative to schist, values less than 1 indicate depletion of an element in pseudotachylyte relative to schist.

(b) Comparison of pseudotachylyte and schist trace element X-ray fluorescence composition. Note depletions in Ga, As, Sr and Y, and enrichments in Rb, Ba and Nb (in pseudotachylyte relative to schist).

Figure 6: (a) Comparison of pseudotachylyte and schist trace element compositions as determined by laser ablation, inductively couple plasma mass spectrometry (LA-ICP-MS). Note Rb and Ba enrichments, and significant depletions in Sr and Eu.

(b) Chrondite normalised REE plot of schist and pseudotachylyte (as determined by LA-ICP-MS). Note significant Eu anomaly, which is only present in pseudotachylyte.

Figure 7: Figure 3: (a) Ar-Ar age spectra for encapsulated stepwise heated sample of "intact rock" pseudotachylyte matrix. (b) Ar-Ar age spectra for unencapsulated stepwise heated sample of pseudotachylyte matrix.

Figure 8: (a) Photo of thin section of OU 74177 displaying flow banding (section length 50 mm).

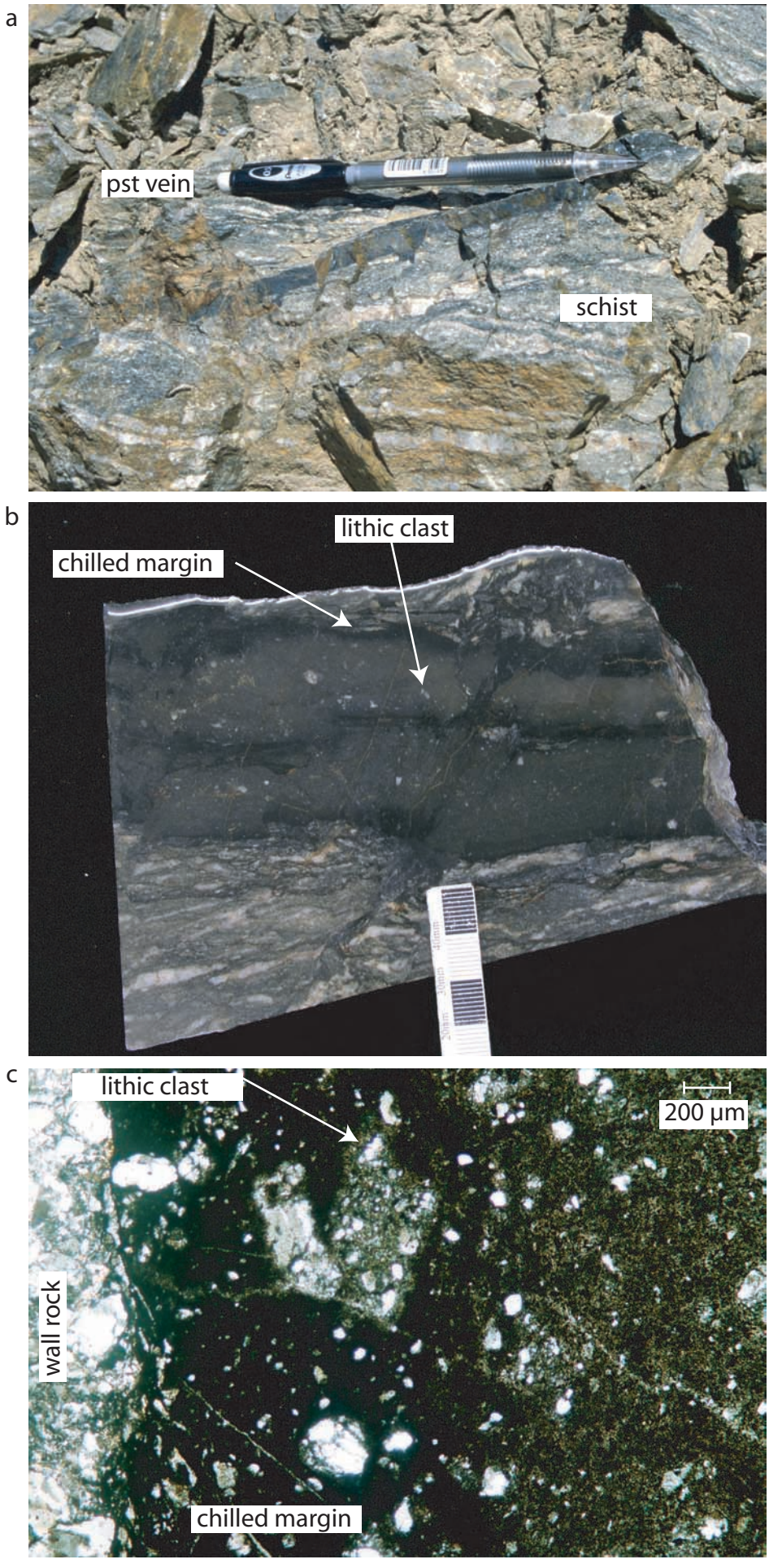
a
pst vein
schist
b
lithic clast
chilled margin
c
lithic clast
200 µm
wall rock
chilled margin

Figure 1

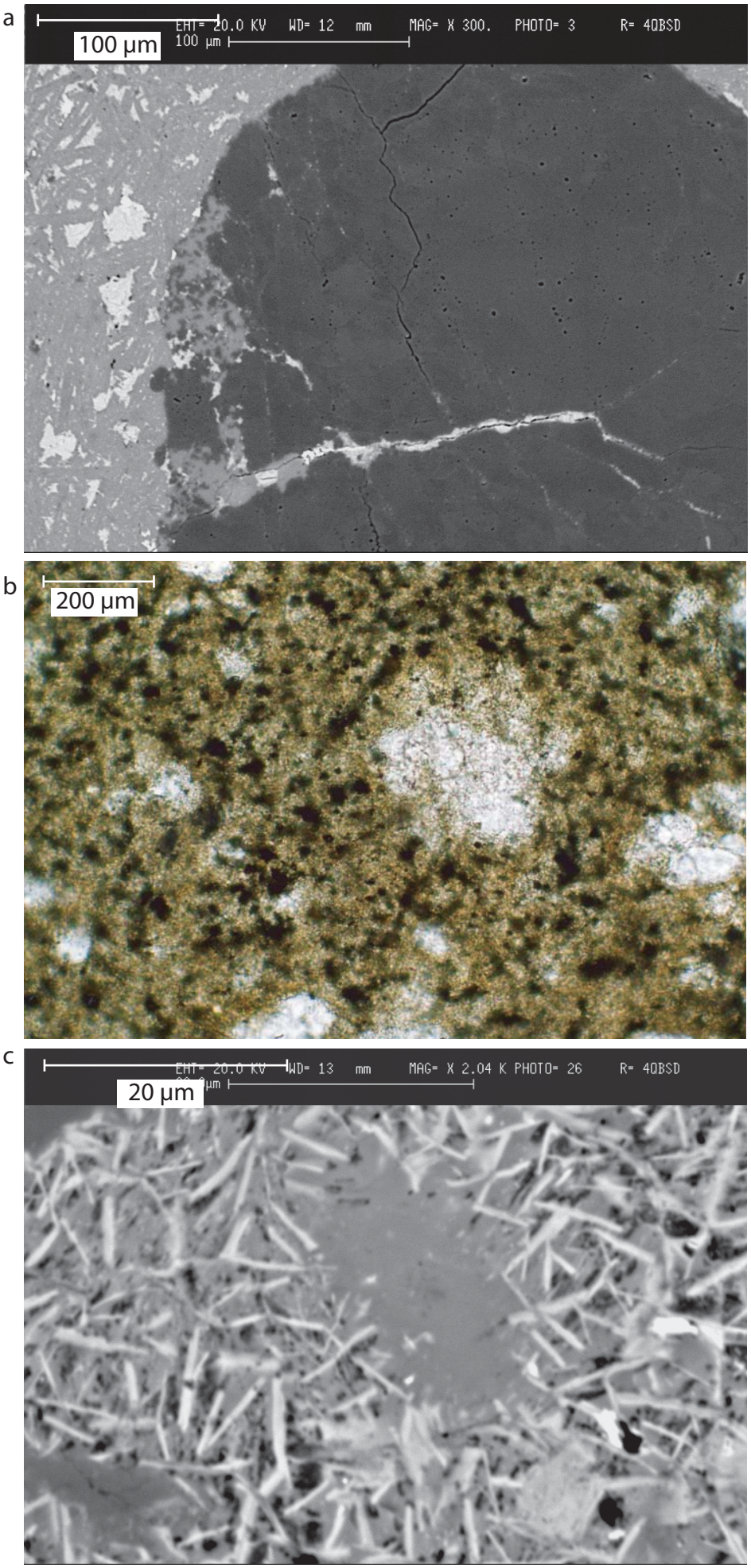
a
EHT= 20.0 KV WD= 12 mm MAG= X 300. PHOTO= 3 R= 40BSD
100 µm
100 µm
b
200 µm
c
EHT= 20.0 KV WD= 13 mm MAG= X 2.04 K PHOTO= 26 R= 40BSD
20 µm

Figure 2

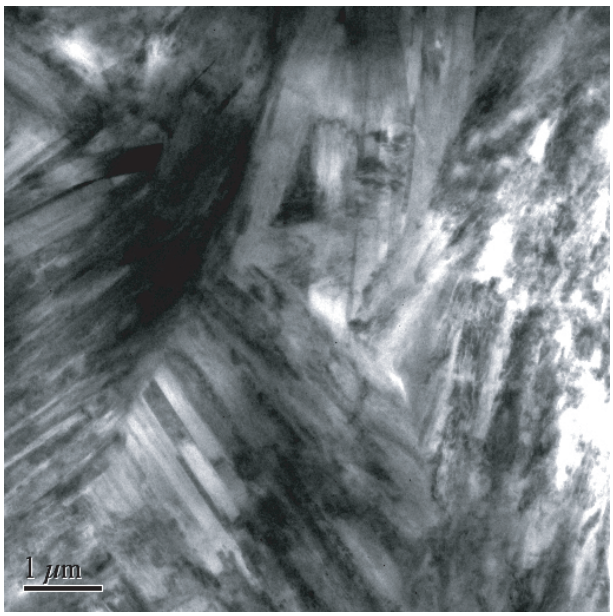


Figure 3

a

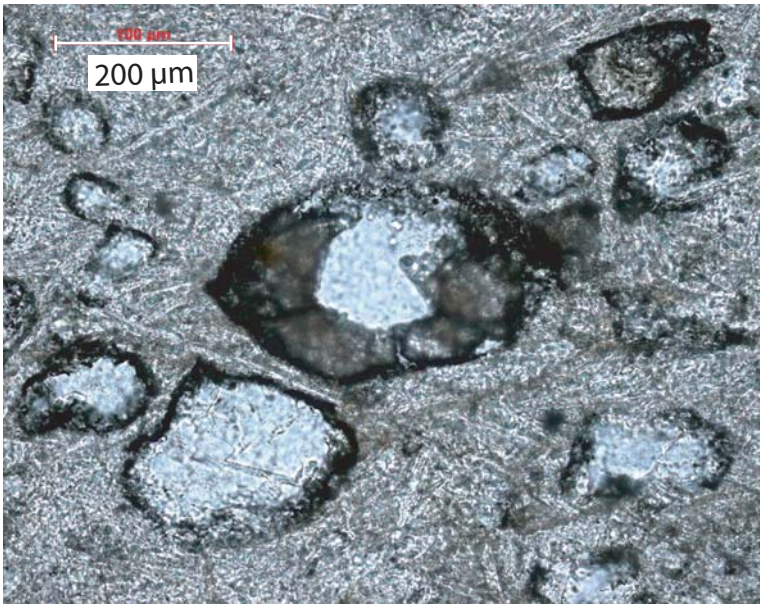


b

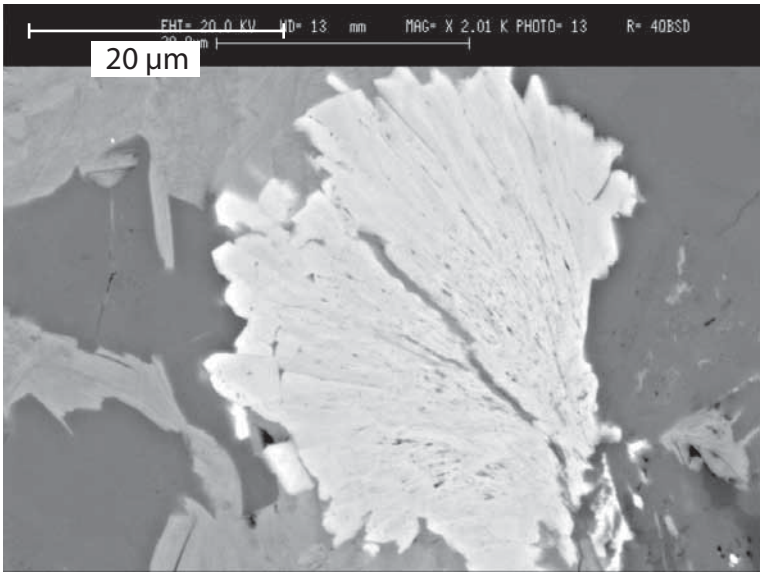


c

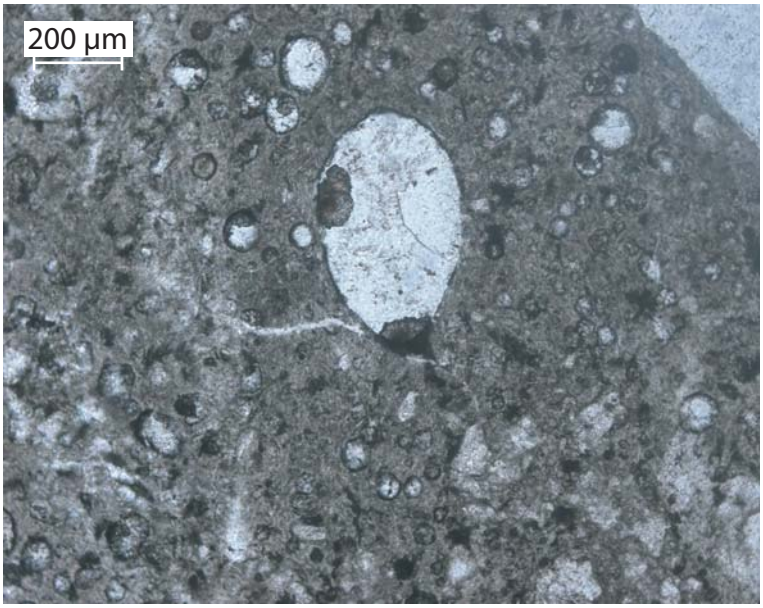


Figure 4

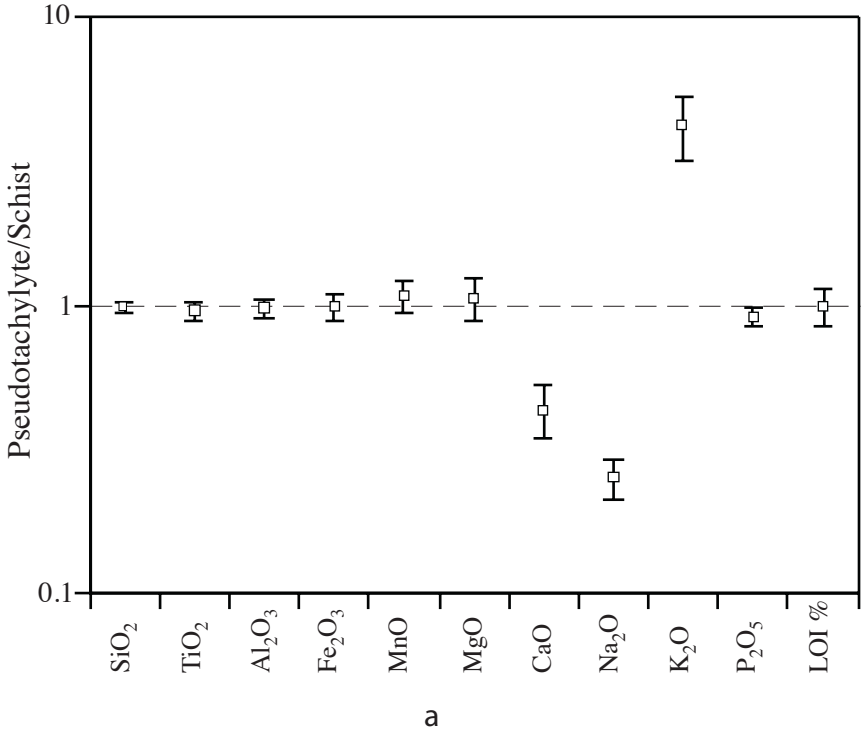
10
1
0.1
Pseudotachylyte/Schist
SiO2
TiO2
Al2O3
Fe2O3
MnO
MgO
CaO
Na2O
K2O
P2O5
LOI %

a

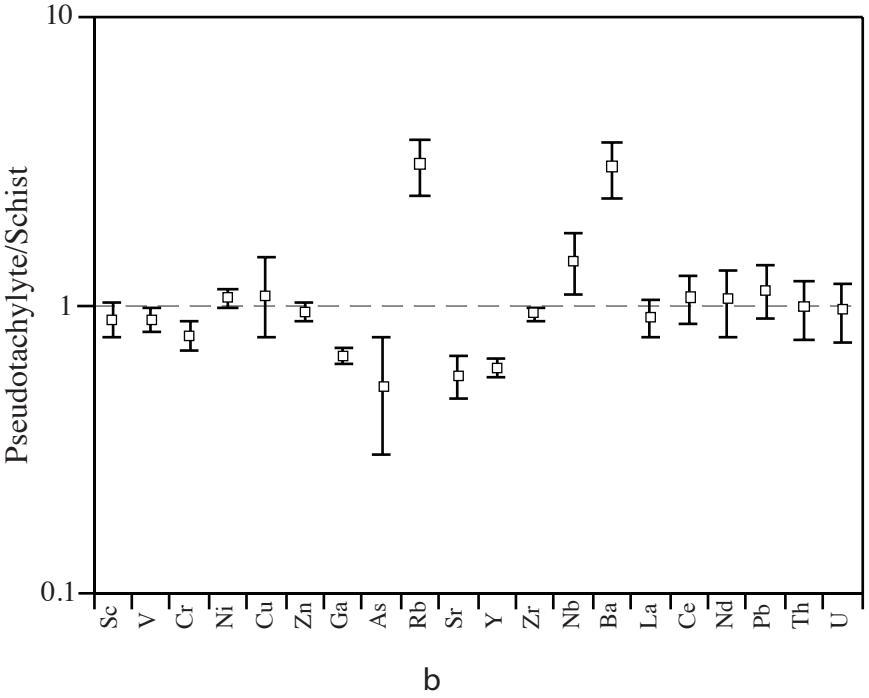
10
1
0.1
Pseudotachylyte/Schist
Sc
V
Cr
Ni
Cu
Zn
Ga
As
Rb
Sr
Y
Zr
Nb
Ba
La
Ce
Nd
Pb
Th
U

b

Figure 5

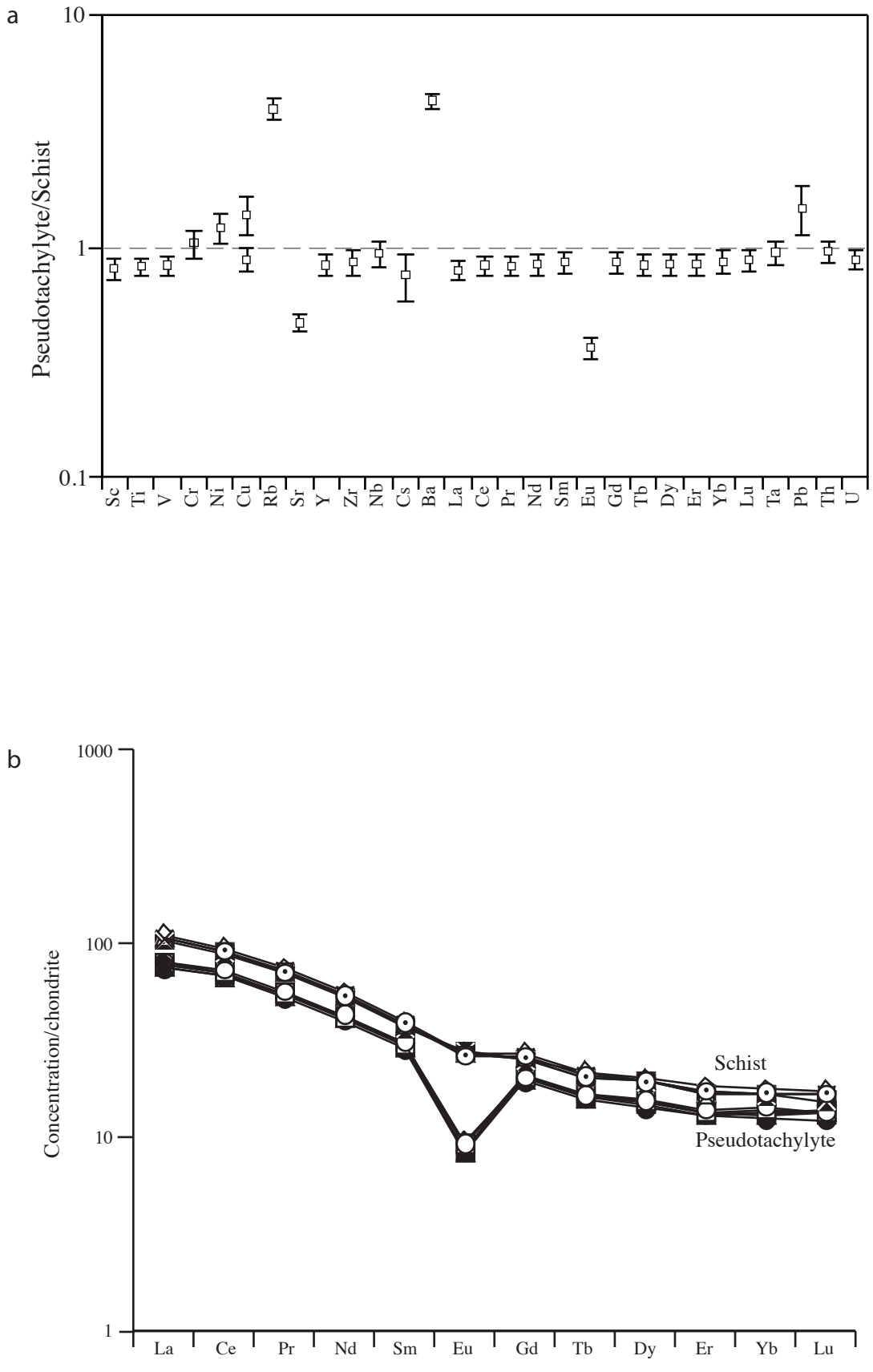
a
10
1
0.1
Pseudotachylyte/Schist
Sc
Ti
V
Cr
Ni
Cu
Rb
Sr
Y
Zr
Nb
Cs
Ba
La
Ce
Pr
Nd
Sm
Eu
Gd
Tb
Dy
Er
Yb
Lu
Ta
Pb
Th
U
b
1000
100
10
1
Concentration/chondrite
Schist
Pseudotachylyte
La
Ce
Pr
Nd
Sm
Eu
Gd
Tb
Dy
Er
Yb
Lu

Figure 6

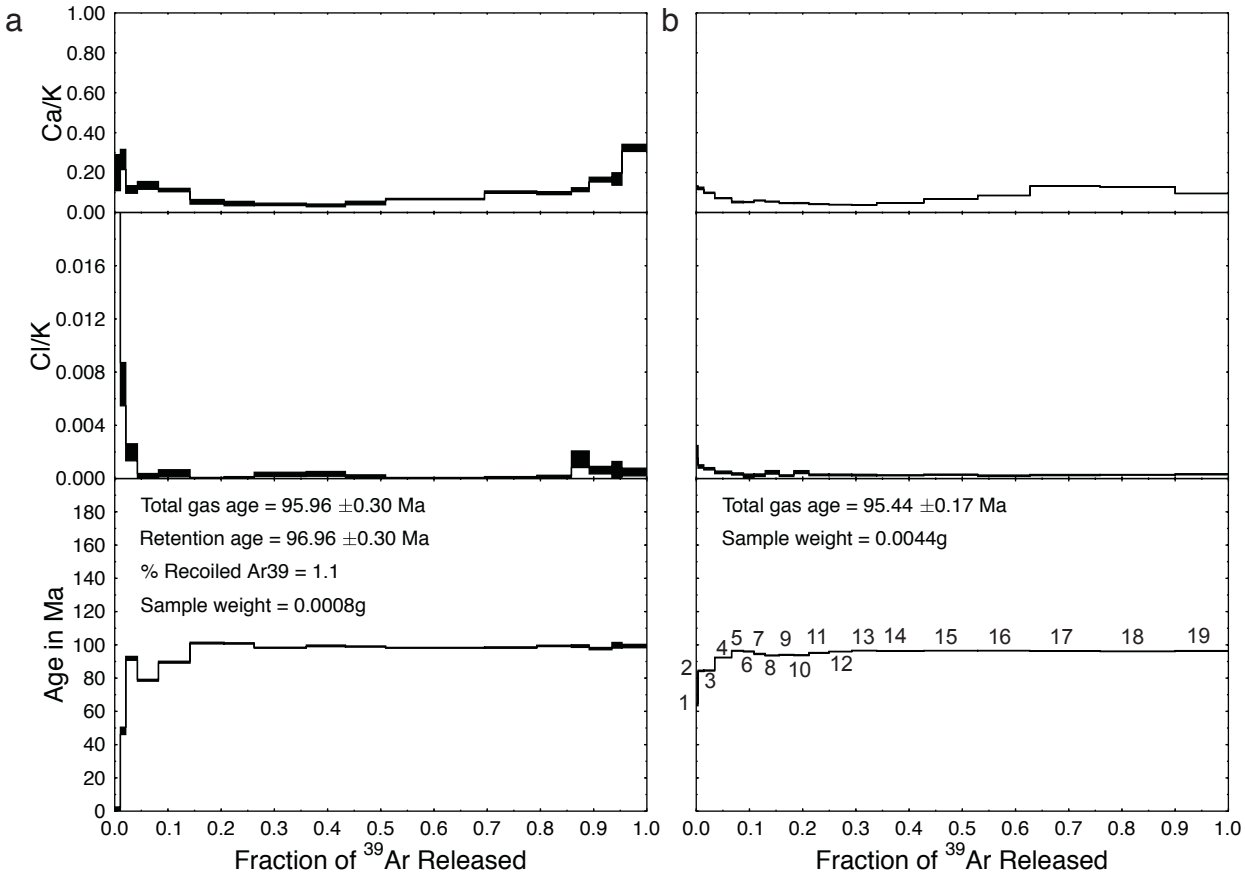
a
b
Ca/K
Cl/K
Age in Ma
Total gas age = 95.96 ±0.30 Ma
Retention age = 96.96 ±0.30 Ma
% Recoiled Ar39 = 1.1
Sample weight = 0.0008g
Total gas age = 95.44 ±0.17 Ma
Sample weight = 0.0044g
Fraction of $^{39}$Ar Released
Fraction of $^{39}$Ar Released

a


Figure 9